INTERNATIONAL JOURNAL FOR NUMERICAL METHODS IN FLUIDS, VOL. 11, 57–86 (1990)

TIME-DEPENDENT NATURAL CONVECTION IN A SQUARE CAVITY: APPLICATION OF A NEW FINITE VOLUME METHOD

HASHIM S. MAHDI AND ROBERT B. KINNEY

Aerospace and Mechanical Engineering Department, University of Arizona, Tucson, AZ 85721, U.S.A.

SUMMARY

A new finite volume (FV) approach with adaptive upwind convection is used to predict the two-dimensional unsteady flow in a square cavity. The fluid is air and natural convection is induced by differentially heated vertical walls. The formulation is made in terms of the vorticity and the integral velocity (induction) law. Biquadratic interpolation formulae are used to approximate the temperature and vorticity fields over the finite volumes, to which the conservation laws are applied in integral form. Image vorticity is used to enforce the zero-penetration condition at the cavity walls. Unsteady predictions are carried sufficiently forward in time to reach a steady state. Results are presented for a Prandtl number (Pr) of 0·71 and Rayleigh numbers equal to 10^3, 10^4 and 10^5. Both 11×11 and 21×21 meshes are used. The steady state predictions are compared with published results obtained using a finite difference (FD) scheme for the same values of Pr and Ra and the same meshes, as well as a numerical bench-mark solution. For the most part the FV predictions are closer to the bench-mark solution than are the FD predictions.

KEY WORDS Finite volume Natural convection Comparison study Numerical methods

INTRODUCTION

In a recent article by the authors[1] a new finite volume approach to solving two-dimensional viscous flow problems was presented. This approach incorporates several ideas which have been developed and used separately by numerical fluid dynamicists over several decades. However, up to the present time they have not been unified into a single and consistent formulation. The new algorithm was developed for steady flows and was applied to two different problems for which there are known exact solutions. The discretization errors were found to be quite small, even when the flow trajectories were inclined steeply to the co-ordinate axes and relatively coarse meshes were used.

These encouraging results have prompted the authors to apply the method to an unsteady viscous flow with sufficient complexities that a fair test of the formulation can be made. Towards this end, we have chosen to analyse the unsteady flow in a square cavity with differentially heated vertical walls. The top and bottom surfaces of the cavity are insulated. De Vahl Davis[2] has developed a bench-mark numerical solution for the steady state flow in this geometry. Thus a set of standard results exist for comparison purposes, at least in the steady state. The extension of our finite volume method to unsteady buoyancy-induced flows together with the results of the numerical predictions for this test problem are the subject of the present paper.

0271–2091/90/090057–30$15.00

Received 26 October 1988
Revised 3 October 1989

We will discuss the previous related works on this test problem subsequently. However, first we present an overview of our numerical approach. The fomulation begins with the integral conservation laws applied to a mesh, the boundaries of which define discrete control volumes within the fluid. This is not a new idea and is often the starting point of control volume formulations which incorporate finite difference methods.[3] The fluid properties transported by the flow are evaluated at single points located interior to the control volumes. We refer to these as 'volume points'. The velocity variables are evaluated at points on the mesh (i.e. control volume boundaries). Thus we have a staggered mesh, which also is not a new feature of the method. We refer to these points on the mesh simply as 'mesh points'. The transported properties (i.e. energy, vorticity, etc.) are approximated over the volumes by biquadratic interpolation functions applied to a nine-node stencil. The velocity variables are approximated over the mesh boundaries by quadratic interpolation functions. The order of both sets of interpolation functions is sufficient to allow accurate evaluation of the variables and their first derivatives over suitably small mesh intervals. The appropriate transport terms in the integral conservation laws are next evaluated and the results integrated over the control volumes in order to obtain discretized versions of the governing flow equations.

There is a remote similarity between the above-described approach and the finite element method, particularly as regards the use of interpolation functions. It is for this reason that we classify it as a finite volume rather than a control volume approach. Although the exact origin of the finite volume method is unknown to the authors, some researchers give credit for introducing the basic idea to MacCormack and Warming.[4] Neither the term 'finite volume' nor the particular algorithm described in the foregoing paragraph can be found in their paper. Rather, procedures are discussed for treating three-dimensional supersonic inviscid flows. Additional citations to finite volume computations of compressible inviscid flows can be found in Reference 1.

In viewing these previous works which use the finite volume method, it is obvious that a great deal of flexibility can be exercised in placing the node points inside and on the surfaces of control volumes. They are not usually staggered and often are located at intersection points (rather than interior points) of the mesh. Also it does not appear to be a requirement that interpolation functions be used to represent the field variables over the mesh.[5] Thus the method seems to lack the kinds of conventions so evident in the finite element and finite difference methods.

A distinguishing feature of the particular finite volume approach used here, and described in Reference 1, is the treatment of the convective transport of the fluid properties (i.e. the advection terms). We use a scheme which is in the category of 'smart upwinding'. Specifically, the transported property is taken to be a volume average of the quantity obtained over a region which is not congruent with a control volume of the mesh, but which is nevertheless located upstream of the one to which the conservation laws are being applied locally. The shape of this region is irregular and depends on the flow trajectory as well as the strength of the convection. It is adaptive to local flow conditions, which can change with space and time.

Upstream-weighted schemes for treating convective transport are controversial and can produce deleterious effects in flow computations. Specifically, it is well known that they introduce numerical (or false) diffusion, as has been documented by many authors (see e.g. References 6–10). Nevertheless, upwind methods are still in use because of their stabilizing influence on the numerical calculations. Furthermore, it is the opinion of the authors that in some situations, even simple (i.e. non-smart first-order) upwind treatments of the convective terms offer a more faithful representation of the flow physics than do central-weighted schemes. This occurs in boundary layer flows, for example, in which the streamwise diffusive transport is entirely negligible and the velocity vector is nearly aligned with one of the co-ordinate axes. Another situation occurs in inviscid transonic flow calculations, for which physically unrealistic expansion shocks can be

avoided by introducing an upwind bias to the convective mass transport in the supersonic zone.[11] Of course in any of these situations the mesh must be properly designed to capture the steep gradients of the flow variables.

Notwithstanding the aforestated examples, there are classes of flows (most notably those with recirculation) for which the numerical diffusion introduced by upwinding is too great to be tolerated, and efforts are being made to improve them. Particularly attractive are the 'smart upwind' schemes which produce solutions to discretized flow problems which agree with the exact solutions for simple (most notably one-dimensional) transport problems. For a discussion of these, see Gresho and Lee.[9] Our scheme has this property as well, but we have extended it to the treatment of two-dimensional flows in a manner which has not previously been proposed.

We now turn to a discussion of the test problem used in the present study. As mentioned previously, a numerical steady state bench-mark solution exists for this buoyancy-induced cavity flow of air (Prandtl number 0·71) in a square cavity.[2] Furthermore, a large body of results for this problem, as obtained using a variety of numerical techniques, can be found in the comparison study by de Vahl Davis and Jones.[12] Results for this test problem continue to appear (and will probably do so for some time) as new techniques are developed for solving the Navier–Stokes equations (see e.g. References 13 and 14).

All of the aforementioned studies are concerned with solving the steady state equations of motion. There are two studies known to the authors which consider the unsteady flow development for this test problem. These were made by Küblbeck *et al.*[15] and Gresho *et al.*[16] In the first of these studies a vorticity–streamfunction formulation was used. Results were presented for two values of the fluid Prandtl number (characteristic of air and water) but only one value of the Grashoff modulus (2×10^4). In the study by Gresho *et al.*[16] a Galerkin finite element method was used and results were given for a Prandtl number of 1·0 and a Rayleigh modulus of 10^5. Both studies report transient as well as steady state results. However, in neither study were the physical parameters the same as those used in References 2 and 12 (which appeared several years later) and on which the present study is based.

The present finite volume approach is applied to the vorticity–velocity formulation in which the velocity field is obtained from the (integral) velocity induction law. Up to the present time this formulation has been used by Kinney and co-workers only to investigate unsteady external flows using a control volume approach. The results of the most recent investigation can be found in the paper by Hung and Kinney.[17] The current investigation is the first time it has been applied to an unsteady internal flow.

ANALYSIS

The analysis is developed for the Cartesian co-ordinate system. The fluid is taken to be viscous and incompressible and is confined to a closed cavity. We assume that the flow is two-dimensional and unsteady. The working equations are developed for the special case of a square cavity, but it is a simple matter to apply the procedures to any rectangular cavity.

The fluid motion is induced by buoyancy effects (i.e. body forces). The vertical walls of the cavity are at different temperatures and the top and bottom surfaces are insulated.

Governing equations

We make use of the well known Boussinesq approximation, a very good account of which is given by Gebhart.[18] The momentum equations are combined into a single equation which governs the transport of the vorticity of the fluid. To this we couple the continuity and energy

equations. The conservation equations for mass, energy and vorticity may thus be written respectively as

$$\frac{\partial u}{\partial x} + \frac{\partial v}{\partial y} = 0, \tag{1}$$

$$\frac{\partial \theta}{\partial t} + \frac{\partial}{\partial x}(u\theta) + \frac{\partial}{\partial y}(v\theta) = \frac{\partial^2 \theta}{\partial x^2} + \frac{\partial^2 \theta}{\partial y^2}, \tag{2}$$

$$\frac{\partial \omega}{\partial t} + \frac{\partial}{\partial x}(u\omega) + \frac{\partial}{\partial y}(v\omega) = RaPr\frac{\partial \theta}{\partial x} + Pr\left(\frac{\partial^2 \omega}{\partial x^2} + \frac{\partial^2 \omega}{\partial y^2}\right). \tag{3}$$

In the foregoing, $Pr = \nu/\alpha$ is the Prandtl number and $Ra = g\beta(T_h - T_c)L^3/\nu\alpha$ is the Rayleigh number, with L the cavity dimension. The thermal diffusivity is α, the kinematic viscosity is ν and β is the isobaric coefficient of thermal expansion. The hot and cold temperatures of the cavity walls are given by T_h and T_c respectively. Except for the temperature, all of the variables have been rendered dimensionless with L and α. The local velocities, then, are similar to local Peclet numbers since they have been divided by α/L. The time variable has been divided by L^2/α, etc. The temperature variable is given by $\theta = (T - T_{avg})/(T_h - T_c)$, where $T_{avg} = 0{\cdot}5(T_h + T_c)$.

A common approach is to eliminate the continuity equation from further consideration by introducing the streamfunction. We pursue an alternative scheme, and to the above equations we add the integral velocity induction law, which is

$$\mathbf{V}(r_P, t) = \frac{1}{2\pi}\int\int_A \frac{\omega_O \times \mathbf{r}_{OP}}{|\mathbf{r}_{OP}|^2}\,dA + \text{grad}\,\phi. \tag{4}$$

This is the general solution (in two dimensions) to the equation $\text{curl}\,\mathbf{V} = \omega$.[17] From this point onwards we will deal only with the scalar magnitude of the vorticity since the vorticity vector has only one component perpendicular to the plane of flow. The term $\text{grad}\,\phi$ in (4) is a purely irrotational contribution to the velocity field and must be added to ensure that the velocity boundary conditions are satisfied. It may be thought of as the velocity field due to image vorticity.[19] In this study we consider that the vorticity ω_O of (4) is located in the square cavity. The image vorticity is located outside the cavity and induces a purely irrotational velocity field at

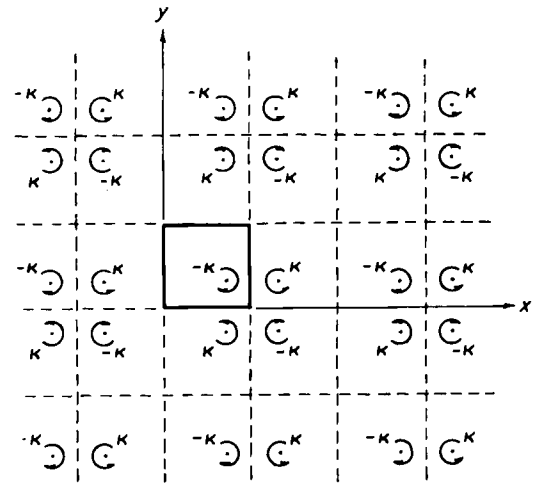

Figure 1. Diagram of image system for free vorticity distribution in the vicinity of the cavity

point P inside it. It is understood that in what follows, the contribution of the image field is included in the expression for the induced velocity so that grad ϕ may be omitted from (4).

The construction of the image vorticity field is straightforward but somewhat tedious. The steps have been carried out in detail in the dissertation[20] on which this paper is based. We give here only a summary of the steps involved.

The superposition principle is used along with results which can be obtained from classical potential flow theory. One first locates a point O inside the cavity. Images of the cavity are drawn which produce a 'checker-board' pattern, and image points to O are located within them. There are in general an infinite number of image points. A portion of the image field near the cavity is shown in Figure 1. The velocity induced at point P inside the cavity by a differential element of the principle vorticity (i.e. $\kappa = \omega \mathrm{d}A$) at point O and all its images is next evaluated. This involves a double infinite sum, one for the horizontal and one for the vertical direction. The infinite sum in the horizontal direction can be evaluated in closed form and involves hyberbolic trigonometric functions. The infinite sum in the vertical direction cannot be reduced to a closed form. As a last step we multiply the expression by the elemental vorticity $\omega \mathrm{d}A$ and integrate over the cavity.

In order to make these results more general, they are stated here for a general rectangular cavity in which W is the width and H is the height. For the horizontal and vertical velocity components we obtain respectively

$$u(x, y, t) = \int_0^H \int_0^W K_{\mathrm{I}}(x, y, \xi, \eta)\, \omega(\xi, \eta, t)\, \mathrm{d}\xi\, \mathrm{d}\eta, \tag{5}$$

$$v(x, y, t) = \int_0^H \int_0^W K_{\mathrm{II}}(x, y, \xi, \eta)\, \omega(\xi, \eta, t)\, \mathrm{d}\xi\, \mathrm{d}\eta. \tag{6}$$

In the foregoing, K_{I} and K_{II} are geometric kernel functions. We let the spatial variables x and y denote the co-ordinates of the point P, and ξ and η denote the co-ordinates of the point O. The kernel functions are given by

$$\begin{aligned} K_{\mathrm{I}} = -\frac{1}{2a}\Bigg[& \frac{\sinh(r_3)\cosh(r_3)}{\sin^2(r_1)+\sinh^2(r_3)} - \frac{\sinh(r_3)\cosh(r_3)}{\sin^2(r_2)+\sinh^2(r_3)} + \frac{\sinh(r_4)\cosh(r_4)}{\sin^2(r_2)+\sinh^2(r_4)} \\ & - \frac{\sinh(r_4)\cosh(r_4)}{\sin^2(r_1)+\sinh^2(r_4)} + \sum_{n=1}^{\infty} \Bigg(\frac{\sinh(r_5)\cosh(r_5)}{\sin^2(r_2)+\sinh^2(r_5)} - \frac{\sinh(r_5)\cosh(r_5)}{\sin^2(r_1)+\sinh^2(r_5)} \\ & + \frac{\sinh(r_6)\cosh(r_6)}{\sin^2(r_1)+\sinh^2(r_6)} - \frac{\sinh(r_6)\cosh(r_6)}{\sin^2(r_2)+\sinh^2(r_6)} + \frac{\sinh(r_7)\cosh(r_7)}{\sin^2(r_1)+\sinh^2(r_7)} \\ & - \frac{\sinh(r_7)\cosh(r_7)}{\sin^2(r_2)+\sinh^2(r_7)} + \frac{\sinh(r_8)\cosh(r_8)}{\sin^2(r_2)+\sinh^2(r_8)} - \frac{\sinh(r_8)\cosh(r_8)}{\sin^2(r_1)+\sinh^2(r_8)} \Bigg) \Bigg], \end{aligned} \tag{7}$$

$$\begin{aligned} K_{\mathrm{II}} = -\frac{1}{2a}\Bigg[& \frac{\sin(r_2)\cos(r_2)}{\sin^2(r_2)+\sinh^2(r_3)} - \frac{\sin(r_1)\cos(r_1)}{\sin^2(r_1)+\sinh^2(r_3)} + \frac{\sin(r_1)\cos(r_1)}{\sin^2(r_1)+\sinh^2(r_4)} \\ & - \frac{\sin(r_2)\cos(r_2)}{\sin^2(r_2)+\sinh^2(r_4)} + \sum_{n=1}^{\infty} \Bigg(\frac{\sin(r_1)\cos(r_1)}{\sin^2(r_1)+\sinh^2(r_5)} - \frac{\sin(r_2)\cos(r_2)}{\sin^2(r_2)+\sinh^2(r_5)} \\ & + \frac{\sin(r_2)\cos(r_2)}{\sin^2(r_2)+\sinh^2(r_6)} - \frac{\sin(r_1)\cos(r_1)}{\sin^2(r_1)+\sinh^2(r_6)} + \frac{\sin(r_2)\cos(r_2)}{\sin^2(r_2)+\sinh^2(r_7)} \\ & - \frac{\sin(r_1)\cos(r_1)}{\sin^2(r_1)+\sinh^2(r_7)} + \frac{\sin(r_1)\cos(r_1)}{\sin^2(r_1)+\sinh^2(r_8)} - \frac{\sin(r_2)\cos(r_2)}{\sin^2(r_2)+\sinh^2(r_8)} \Bigg) \Bigg]. \end{aligned} \tag{8}$$

The quantities r_i, $i = 1, \ldots, 8$, are as follows:

$$r_1 = \frac{\pi}{a}(x - \xi), \qquad r_2 = \frac{\pi}{a}(x + \xi), \tag{9a}$$

$$r_3 = \frac{\pi}{a}(y - \eta), \qquad r_4 = \frac{\pi}{a}(y + \eta), \tag{9b}$$

$$r_5 = \frac{\pi}{a}(y - P_1), \qquad r_6 = \frac{\pi}{a}(y + P_1), \tag{9c}$$

$$r_7 = \frac{\pi}{a}(y - P_2), \qquad r_8 = \frac{\pi}{a}(y + P_2), \tag{9d}$$

where $P_1 = 2nH - \eta$, $P_2 = 2nH + \eta$ and $a = 2W$. To apply these results to the present study we set $W = H = L = 1$.

It may be shown that the foregoing expressions for u and v will yield zero components of velocity perpendicular to the cavity walls. However, the tangential component will not necessarily be zero. Since we need to enforce the viscous adherence condition, a tangential 'slip' velocity cannot be tolerated. This is reduced to zero in the calculations by the proper production of vorticity at the solid boundaries. This is in keeping with the concept originally proposed by Lighthill[19] and used previously by Kinney and co-workers. See Reference 17 for citations to these works. The vorticity production algorithm involves the numerical boundary condition for the vorticity transport equation. This will be discussed in the section dealing with the numerical methods.

The air is initially at rest and has uniform temperature. Thus the initial conditions imposed on the aforestated governing equations require that $\omega(x, y, 0) = \theta(x, y, 0) = 0$. For $t > 0$ we have for the boundary conditions:

$$\theta(0, y, t) = 0{\cdot}5, \quad \theta(1, y, t) = -0{\cdot}5 \quad \text{and} \quad (\partial\theta/\partial y)(x, 0, t) = (\partial\theta/\partial y)(x, 1, t) = 0.$$

The boundary conditions on the velocity and vorticity have been discussed in the previous paragraph.

Nusselt number

In order to characterize the heat transfer results, we use a pseudo-heat flux which is defined to be the sum of the enthalpy transport plus the molecular conduction. The x-component of this heat flux is given by

$$Q_x = \rho C_p u(T - T_{avg}) - k\frac{\partial T}{\partial x}. \tag{10}$$

Here ρ is the fluid density, C_p is the specific heat at constant pressure and k is the thermal conductivity. Also T_{avg} is the reference temperature for the enthalpy. The heat transfer coefficient $\hat{h}$ is defined in terms of Q_x anywhere in the fluid, and not just its value at the hot or cold surfaces. This is in keeping with the definition used in References 2 and 12, but it does depart from the usual convention. That is, $\hat{h} \equiv Q_x/(T_h - T_c)$. We now introduce dimensionless variables as previously defined, as well as the Nusselt number Nu. Thus

$$Nu \equiv \frac{\hat{h}L}{k} = u\theta - \frac{\partial\theta}{\partial x}. \tag{11}$$

In order to obtain results comparable to those reported in Reference 2, and preserving essentially the same notion, we introduce values for Nu_x evaluated at any vertical plane within the cavity. That is,

$$Nu_x = \int_0^1 \left(u\theta - \frac{\partial \theta}{\partial x} \right) \mathrm{d}y. \tag{12}$$

Specific results of interest are Nu_0 and $Nu_{1/2}$, where in (12) we use $x = 0$ and 0·5 respectively.

Finally, a spatial average for the Nusselt number over the whole cavity is given by

$$\overline{Nu} = \int_0^1 \int_0^1 \left(u\theta - \frac{\partial \theta}{\partial x} \right) \mathrm{d}x\, \mathrm{d}y. \tag{13}$$

We note in passing that since the top and bottom surfaces of the cavity are insulated, the integrated Nusselt number along any vertical plane spanning the cavity must be the same for each x. In particular, $Nu_0 = Nu_{1/2}$. It follows that $\overline{Nu}$ must equal these same values as well.

Conservation law for total vorticity

We next introduce an integral conservation law for the total vorticity. To the authors' knowledge, this law has not previously been derived for this cavity problem. It can be obtained by integrating the momentum equations around the closed contour which is coincident with the walls of the cavity. The continuity equation is also used to eliminate some of the terms. Since the pressure term is an exact differential, the integral of it must vanish for any closed contour. Also the enforcement of the viscous adherence condition ensures that the unsteady momentum terms vanish on the contour. The body force term in the y-component of the momentum equation is written $-\rho g$. The density may be considered to be a variable. That is, it is not necessary to invoke the Boussinesq approximation. However, the dynamic viscosity of the fluid, μ, is taken to be a constant.

As was the case previously, we state the results for a rectangular cavity of width W and height H. Also dimensional quantities are used. The result is

$$0 = -g \int_0^H (\rho(0,y,t) - \rho(W,y,t))\mathrm{d}y + \mu \int_0^H \left(\frac{\partial \omega}{\partial x}(0,y,t) - \frac{\partial \omega}{\partial x}(W,y,t) \right) \mathrm{d}y$$
$$+ \mu \int_0^W \left(\frac{\partial \omega}{\partial y}(x,0,t) - \frac{\partial \omega}{\partial y}(x,H,t) \right) \mathrm{d}x. \tag{14}$$

Note that the foregoing expression is valid for unsteady flows.

We next invoke the Boussinesq approximation and write

$$\rho(0,y,t) - \rho(W,y,t) = -\rho^* \beta (T(0,y,t) - T(W,y,t)) = -\rho^* \beta (T_h - T_c) = \text{constant}. \tag{15}$$

Note that ρ^* is a reference density which is considered to be constant. We simply write this now as ρ. The final step is to non-dimensionalize the variables in the manner previously noted. We also set $W = H = L$ and obtain

$$0 = RaPr + Pr \int_0^1 \left(\frac{\partial \omega}{\partial x}(0,y,t) - \frac{\partial \omega}{\partial x}(1,y,t) \right) \mathrm{d}y + Pr \int_0^1 \left(\frac{\partial \omega}{\partial y}(x,0,t) - \frac{\partial \omega}{\partial y}(x,1,t) \right) \mathrm{d}x. \tag{16}$$

This is the form of the conservation law for total vorticity to be used in this analysis. It states that the net surface production of positive vorticity of the four cavity walls must equal the net volumetric production of negative vorticity by the body forces. That is, the production of total

vorticity is zero. Since it starts out with value zero when the fluid is at rest, it remains zero for all time. This can be verified by integrating equation (3) over the whole cavity and making use of (16).

Scaling parameter for the velocity and vorticity

We seek a scaling factor for the dimensionless velocity and vorticity variables. The temperature variable is already properly scaled. It is reasonable to expect that these will be proportional to some power of the Rayleigh number. Gebhart[18] uses a simple but intuitive estimate to reason that the velocities should scale as $Ra^{1/2}$. This should also be true of the vorticity. Therefore we introduce the scaled variables $\tilde{u} = u/(Ra)^{1/2}$, $\tilde{v} = v/(Ra)^{1/2}$ and $\tilde{\omega} = \omega/(Ra)^{1/2}$. When these are introduced into equations (1)–(3) we obtain

$$\frac{1}{(Ra)^{1/2}}\left(\frac{\partial \tilde{u}}{\partial x} + \frac{\partial \tilde{v}}{\partial y}\right) = 0, \tag{17}$$

$$\frac{1}{Ra}\frac{\partial \theta}{\partial t} + \frac{1}{(Ra)^{1/2}}\left(\frac{\partial}{\partial x}(\tilde{u}\theta) + \frac{\partial}{\partial y}(\tilde{v}\theta)\right) = \frac{1}{Ra}\left(\frac{\partial^2 \theta}{\partial x^2} + \frac{\partial^2 \theta}{\partial y^2}\right), \tag{18}$$

$$\frac{1}{Ra}\frac{\partial \tilde{\omega}}{\partial t} + \frac{1}{(Ra)^{1/2}}\left(\frac{\partial}{\partial x}(\tilde{u}\tilde{\omega}) + \frac{\partial}{\partial y}(\tilde{v}\tilde{\omega})\right) = \frac{Pr}{(Ra)^{1/2}}\frac{\partial \theta}{\partial x} + \frac{Pr}{Ra}\left(\frac{\partial^2 \tilde{\omega}}{\partial x^2} + \frac{\partial^2 \tilde{\omega}}{\partial y^2}\right). \tag{19}$$

We note here that the corresponding terms in these equations are all similar. In particular, the coefficients of the unsteady terms are $1/Ra$, the coefficients of the convective and buoyancy terms are $1/Ra^{1/2}$ and the coefficients of the diffusive terms are $1/Ra$. This point will be exploited in the next section when the numerical methods are presented. Specifically, it will lead to a rationale for choosing the discrete time and distance steps for various Rayleigh numbers.

NUMERICAL METHODS

We begin with the governing equations (1)–(3). All terms are transposed to the left-hand side, following which they are integrated over a typical control volume. This will be taken to lie in the region given by $x_1 \le x \le x_2$ and $y_1 \le y \le y_2$. Note that the convective transport terms are all written in the so-called 'conservative' or 'divergence' form. That is also true of the diffusive terms. Thus these terms produce integrals over the boundaries of the control volumes. Following the spatial integration, equations (2) and (3) are integrated with respect to time from t to $t + \Delta t$. Both of these operations produce exact expressions. We thus obtain

$$\int_{y_1}^{y_2} (u(x_2, y, t) - u(x_1, y, t))\,dy + \int_{x_1}^{x_2} (v(x, y_2, t) - v(x, y_1, t))\,dx = 0, \tag{20}$$

$$\int_{y_1}^{y_2}\int_{x_1}^{x_2} (\theta(t + \Delta t, x, y) - \theta(t, x, y))\,dx\,dy + \int_{t}^{t+\Delta t}\left(\int_{y_1}^{y_2} ([u\theta](x_2, y, t) - [u\theta](x_1, y, t))\,dy + \int_{x_1}^{x_2} ([v\theta](x, y_2, t) - [v\theta](x, y_1, t))\,dx\right)dt - \int_{t}^{t+\Delta t}\left[\int_{y_1}^{y_2}\left(\frac{\partial \theta}{\partial x}(x_2, y, t) - \frac{\partial \theta}{\partial x}(x_1, y, t)\right)dy + \int_{x_1}^{x_2}\left(\frac{\partial \theta}{\partial y}(x, y_2, t) - \frac{\partial \theta}{\partial y}(x, y_1, t)\right)dx\right]dt = 0, \tag{21}$$

$$\int_{y_1}^{y_2}\int_{x_1}^{x_2}(\omega(t+\Delta t,x,y)-\omega(t,x,y))\,dx\,dy+\int_t^{t+\Delta t}\left(\int_{y_1}^{y_2}([u\omega](x_2,y,t)-[u\omega](x_1,y,t))\,dy\right.$$
$$\left.+\int_{x_1}^{x_2}([v\omega](x,y_2,t)-[v\omega](x,y_1,t))\,dx\right)dt-Pr\int_t^{t+\Delta t}\left[\int_{y_1}^{y_2}\left(\frac{\partial\omega}{\partial x}(x_2,y,t)-\frac{\partial\omega}{\partial x}(x_1,y,t)\right)dy\right.$$
$$\left.+\int_{x_1}^{x_2}\left(\frac{\partial\omega}{\partial y}(x,y_2,t)-\frac{\partial\omega}{\partial y}(x,y_1,t)\right)dx\right]dt-RaPr\int_t^{t+\Delta t}\left(\int_{y_1}^{y_2}(\theta(x_2,y,t)-\theta(x_1,y,t))\,dy\right)dt$$
$$=0. \qquad (22)$$

We have adopted the following notation: $[\ldots](x, y, t)$ means that all quantities inside the square brackets have the argument (x, y, t). To proceed further, some level of approximation must be made, and to this end we apply the finite volume formulation described in the next section.

Finite volume formulation

The basic approach has already been described in Reference 1 and some of the derived expressions carry over directly to the present work. Complete derivations are given in Reference 20.

A typical mesh for the square cavity is shown in Figure 2. In this illustration the volume points are not shown, but away from the boundaries of the cavity these would appear at the centres of squares defined by the dotted lines of the mesh. On the cavity boundaries they would be midway between mesh lines. There are also volume points at the four corners of the cavity. A 21 × 21 mesh is shown. The dimension of each square control volume is h on a side. Thus h is also the distance between volume points.

A typical finite volume with the nodal arrangement is shown in Figure 3. The volume points at which the temperature and vorticity are evaluated are shown as '×'s inside circles and are numbered 1–9 (also $i-1, j-1$ to $i+1, j+1$) for easy reference. The mesh points at which the horizontal velocity components are evaluated are shown as '+'s inside squares, and those at

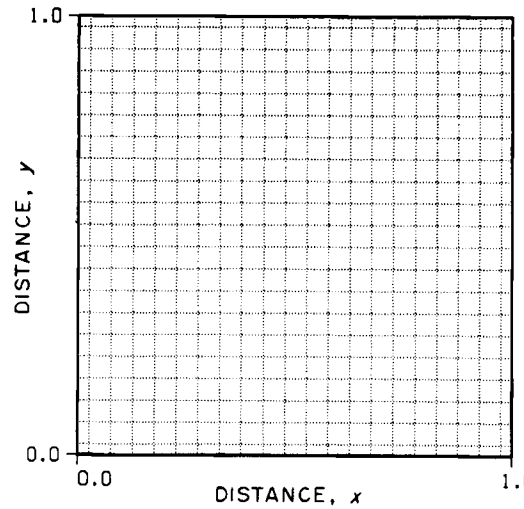

Figure 2. Diagram of the 21 × 21 mesh configuration for the cavity, $h = 0{\cdot}05$

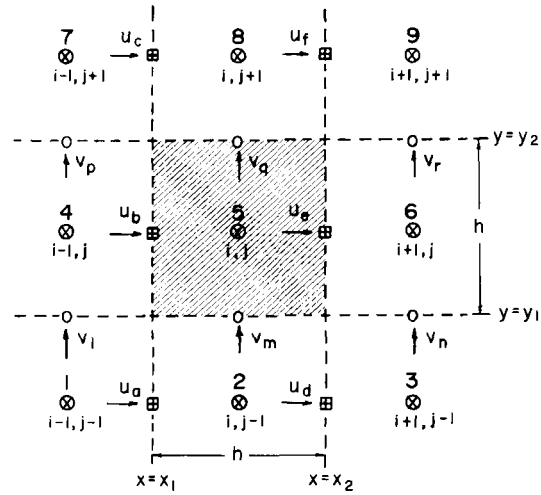

Figure 3. Diagram of control volume showing node point arrangement

which the vertical velocity are evaluated are shown as open circles. The control volume is bounded by co-ordinate lines x_1, x_2, y_1 and y_2.

The temperature and vorticity variables are approximated by biquadratic interpolation functions as follows:

$$\theta(x, y, t) \simeq \sum_{k=1}^{9} N^k(x, y)\,\theta_k(t), \tag{23}$$

$$\omega(x, y, t) \simeq \sum_{k=1}^{9} N^k(x, y)\,\omega_k(t). \tag{24}$$

The horizontal velocity component is approximated by a simple quadratic function as follows:

$$u(x_n, y, t) \simeq \sum_{k=1}^{3} N_k(y)\,u_k(x_n, t), \tag{25}$$

where $n = 1, 2$ and N^k, N_k are given in Reference 1. The vertical velocity component is evaluated using a different procedure and will be described subsequently.

These expressions are next substituted into equations (20)–(22) and the integrations are carried out. The pertinent results are given in the next sections.

We note here that the basic formulation is not dependent on the specific approach used to determine the velocity field. It is only required that the horizontal components of velocity be evaluated at the mesh points, as described above. Thus, for example, a stream function formulation could also be used, but for consistency it would be necessary to develop it along the lines presented here.

Continuity equation

In the convective transport algorithm, to be described later, the volumetric flow rates across the faces of the control volume are needed. These are found by the procedure already described in Reference 1, which will only be summarized here.

The horizontal components of velocity at each mesh point are first evaluated from equation (5). These are then interpolated by quadratic formulae and the volumetric flow rates across vertical

faces of the control volumes are found by integration. The volumetric flow rates across horizontal faces of the control volume are found by enforcing conservation of mass. One begins at the bottom of the cavity and marches in the vertical direction, ending at the top.

There are, however, two situations in which the vertical velocity components themselves are needed, for which equation (6) is used. These are used to construct the velocity profile at the horizontal midplane of the cavity and to find the 'slip' velocities along the vertical walls of the cavity. The latter appears in the numerical boundary condition for the vorticity transport equation and will be discussed subsequently. The numerical procedure used to evaluate (5) and (6) will be discussed in a later section.

We denote by $\dot{V}_{i,j}(x_2, t)$ the volumetric flow rate across the right-hand vertical face. The subscript i, j refers to the node on which the control volume is centred, and the argument denotes the plane across which the fluid is passing. Thus $\dot{V}_{i,j}(y_1, t)$ is the volumetric flow rate across the lower horizontal face of the same control volume.

Note that this procedure ensures mass flux consistency plus local conservation of mass. However, it does not guarantee that the volumetric flow rate across the impermeable top of the cavity is zero. Nevertheless, this quantity was checked during the course of the computations and found to be negligibly small (i.e. $O(10^{-6})$).

As an alternative to the present procedure, one could use both equations (5) and (6) to evaluate respectively the horizontal and vertical components of velocity at mesh points on the sides of the control volumes, following which the volumetric flow rates could be found by integration. However, there is no guarantee that mass will be conserved locally on the descrete mesh, since several levels of approximation are used in evaluating (5) and (6) and the subsequent integrations. It can be shown that the integral velocity formulation does produce an exactly solenoidal velocity field, but only in the limit of a vanishingly small control volume. Although the continuity errors might be acceptably small on a fine mesh, the present procedure is preferrable because it is computationally more efficient and does ensure local mass conservation on even a coarse mesh.

Vorticity transport equation

Except for the buoyancy term in equation (3), the vorticity transport and energy equations are identical. Therefore the general discussion will be limited to the terms in the former equation only. A few special considerations needed in treating the energy equation will be discussed in a later section.

Storage term. The storage term is described first. We have for an interior control volume the result

$$\int_{y_1}^{y_2}\int_{x_1}^{x_2} \omega(t + \Delta t, x, y)\,dx\,dy \simeq \sum_{k=1}^{9} \omega_k(t + \Delta t) \int_{y_1}^{y_2}\int_{x_1}^{x_2} N^k(x, y)\,dx\,dy$$

$$\frac{h^2}{576}(\omega_1^+ + 22\omega_2^+ + \omega_3^+ + 22\omega_4^+ + 484\omega_5^+ + 22\omega_6^+ + \omega_7^+ + 22\omega_8^+ + \omega_9^+). \tag{26}$$

We use the notation that $\omega_k(t + \Delta t) = \omega_k^+, k = 1, \ldots, 9$. The result for time level t is the same as that given above with the '+' omitted from the vorticity terms.

Since the values of the vorticity at all volume points residing on the cavity boundary are not known *a priori*, they are found from the governing transport equation applied to these control volumes. Thus terms analogous to (26) must be evaluated. However, cognizance must be taken of the fact that the dimensions of the relevant control volumes are no longer $h \times h$. The various

results are too numerous to give here, and the reader is referred to Reference 20 for detailed listings of these. This will be the case for all the transport terms to be considered in this section which apply to control volumes adjacent to the boundary.

Diffusive terms. The diffusive terms are evaluated next. These, as well as all the remaining terms, involve integrals over the surfaces of the control volumes as well as over the time interval t to $t + \Delta t$. The spatial integration is carried out in closed form but the temporal integration is approximated using the trapezoidal rule. This has a truncation error $O(\Delta t^3)$. The total of the diffusion transport terms in equation (22) is

$$Pr\int_t^{t+\Delta t}\left[\int_{y_1}^{y_2}\left(\frac{\partial\omega}{\partial x}(x_2, y, t) - \frac{\partial\omega}{\partial x}(x_1, y, t)\right)dy + \int_{x_1}^{x_2}\left(\frac{\partial\omega}{\partial y}(x, y_2, t) - \frac{\partial\omega}{\partial y}(x, y_1, t)\right)dx\right]dt$$
$$= Pr\frac{\Delta t}{2}\frac{1}{576}[48(\omega^+ + \omega)_1 + 480(\omega^+ + \omega)_2 + 48(\omega^+ + \omega)_3 + 480(\omega^+ + \omega)_4$$
$$- 2112(\omega^+ + \omega)_5 + 480(\omega^+ + \omega)_6 + 48(\omega^+ + \omega)_7 + 480(\omega^+ + \omega)_8 + 48(\omega^+ + \omega)_9]. \tag{27}$$

Note that the use of biquadratic interpolation formulae ensures that there is diffusive flux consistency on a uniform mesh such as that used in the present study.

Buoyancy term. We next turn to the consideration of the buoyancy term. For any interior control volume the total buoyancy term is

$$RaPr\int_t^{t+\Delta t}\left(\int_{y_1}^{y_2}(\theta(x_2, y, t) - \theta(x_1, y, t))dy\right)dt \simeq RaPr\frac{\Delta t}{2}\frac{h}{576}[-12(\theta^+ + \theta)_1 + 12(\theta^+ + \theta)_3$$
$$- 264(\theta^+ + \theta)_4 + 264(\theta^+ + \theta)_6 - 12(\theta^+ + \theta)_7 + 12(\theta^+ + \theta)_9]. \tag{28}$$

Convective terms. The convective terms are discussed next. This involves a special 'upstream-weighted' scheme. The idea is to equate the convective transport to the product of the volumetric flow rate and a specially defined volumetric average of the vorticity. We have, for example,

$$\int_t^{t+\Delta t}\left(\int_{y_1}^{y_2}[u\omega](x_2, y, t)dy\right)dt \simeq \frac{\Delta t}{2}\int_{y_1}^{y_2}[(u\omega)^+ + (u\omega)](x_2, y)dy$$
$$\simeq \frac{\Delta t}{2}[\hat{\omega}^+ + \hat{\omega}](x_2)\int_{y_1}^{y_2}u(x_2, y, t)dy$$
$$\simeq \frac{\Delta t}{2}[\hat{\omega}^+ + \hat{\omega}](x_2)\dot{V}_{i,j}(x_2, t). \tag{29}$$

For the convective transport in the vertical direction we have

$$\int_t^{t+\Delta t}\left[\int_{x_1}^{x_2}[v\omega](x, y_2, t)dx\right]dt \simeq \frac{\Delta t}{2}[\hat{\omega}^+ + \hat{\omega}](y_2)\dot{V}_{i,j}(y_2, t). \tag{30}$$

Observe that the velocities u as well as the volumetric flow rates in the vertical direction are evaluated at time level t. The vorticity values are evaluated at two time levels, t and $t + \Delta t$. This mixed-time-level scheme avoids a non-linearity in the discretized vorticity transport equation. However, this is at the expense of a larger-order truncation error in the convective terms than would be the case if a true trapezoidal rule were used for the time integration.

The quantity $\hat{\omega}$ is the volumetric average of the vorticity crossing the control surfaces. It is defined over a trapezoidal region which adjoins a control volume at one of the surfaces. An illustration of this is given by the cross-hatched region in Figure 4. The width of the trapezoid is a factor D_{opt} times h.

The algorithm for determining D_{opt} is derived from consideration of a steady state one-dimensional convection–diffusion problem on a domain with specified endpoint values of the dependent variable. It is a function of the cell Peclet number Pe_h, evaluated at the centres of the four faces of the control volume shown in Figure 3. There are thus four values of the cell Peclet number. For dimensional values of the velocities and spatial increment these are given by $u_b h/\alpha$, $u_e h/\alpha$, $v_m h/\alpha$ and $v_q h/\alpha$. Note that here we use $v_m = (1/h)\dot{V}_{i,j}(y_1, t)$ and $v_q = (1/h)\dot{V}_{i,j}(y_2, t)$. The four different values for D_{opt} are then determined from

$$D_{opt} = \coth\frac{Pe_h}{2} - \frac{2}{Pe_h}. \tag{31}$$

The foregoing expression is a convenient algorithm for determining the 'optimum' distance factor. It has the advantage that it varies locally with the strength of the convection. Therefore it adjusts automatically to the evolving flow conditions and needs no analyst intervention during the course of the calculations. Other algorithms could conceivably be envisioned, but it is the only one considered in this study.

Discrete form of the vorticity transport equation

All of the terms described in the preceding sections are substituted into equation (22). After rearrangement we obtain, for a nine-node stencil centred on an interior control volume, the linear equation

$$\begin{aligned}
&\omega_1^+(C_1 - 48C_2) + \omega_2^+(22C_1 - 480C_2) + \omega_3^+(C_1 - 48C_2) + \omega_4^+(22C_1 - 480C_2)\\
&\quad + \omega_5^+(484C_1 + 2112C_2) + \omega_6^+(22C_1 - 480C_2) + \omega_7^+(C_1 - 48C_2) + \omega_8^+(22C_1 - 480C_2)\\
&\quad + \omega_9^+(C_1 - 48C_2) + \frac{\Delta t}{2}([\hat{\omega}^+](x_2)\dot{V}_{i,j}(x_2, t) - [\hat{\omega}^+](x_1)\dot{V}_{i,j}(x_1, t)\\
&\quad + [\hat{\omega}^+](y_2)\dot{V}_{i,j}(y_2, t) - [\hat{\omega}^+](y_1)\dot{V}_{i,j}(y_1, t))\\
&= \omega_1(C_1 + 48C_2) + \omega_2(22C_1 + 480C_2) + \omega_3(C_1 + 48C_2)\\
&\quad + \omega_4(22C_1 + 480C_2) + \omega_5(484C_1 - 2112C_2) + \omega_6(22C_1 + 480C_2)\\
&\quad + \omega_7(C_1 + 48C_2) + \omega_8(22C_1 + 480C_2) + \omega_9(C_1 + 48C_2)\\
&\quad - \frac{\Delta t}{2}([\hat{\omega}](x_2)\dot{V}_{i,j}(x_2, t) - [\hat{\omega}](x_1)\dot{V}_{i,j}(x_1, t) + [\hat{\omega}](y_2)\dot{V}_{i,j}(y_2, t) - [\hat{\omega}](y_1)\dot{V}_{i,j}(y_1, t))\\
&\quad + RaPr\frac{\Delta t}{2}\frac{C_1}{h}[-12(\theta^+ + \theta)_1 + 12(\theta^+ + \theta)_3 - 264(\theta^+ + \theta)_4\\
&\quad + 264(\theta^+ + \theta)_6 - 12(\theta^+ + \theta)_7 + 12(\theta^+ + \theta)_9],
\end{aligned} \tag{32}$$

where $C_1 = h^2/576$ and $C_2 = \Delta t Pr/1152$.

Observe that the volume-averaged vorticities transported by the flow (i.e. $\hat{\omega}$) are shown separately. These contain values of the vorticity evaluated at the nine nodes surrounding the control volume. However, the values of the coefficients are not known *a priori* since they depend

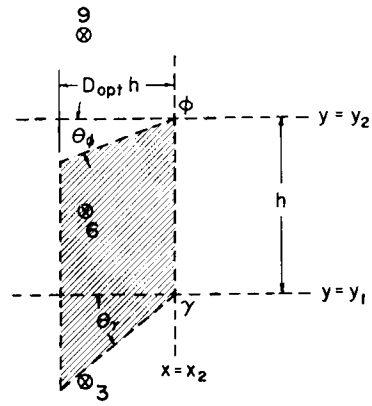

Figure 4. Trapezoidal region over which volume average of convected property is computed

on the local flow trajectories and the strength of the convection. These coefficients have to be evaluated during the course of the calculations and then assembled with those of the other terms in the equation.

Equation (32) must be modified for control volumes which lie adjacent to the cavity wall. This is because the vorticity production at solid surfaces, which arises through enforcement of the viscous adherence condition, has not been accounted for. We illustrate the procedure here for only one control volume. Reference 20 contains a full discussion of the required modifications for all the affected equations.

The numerical model for vorticity production at a solid wall is given by

$$Pr\int_t^{t+\Delta t}\left.\frac{\partial\omega}{\partial n}\right|_{\text{wall}}\mathrm{d}t' = \pm U_{\text{slip}}(s, t), \tag{33}$$

where s denotes a generalized co-ordinate on the wall. Background discussion pertaining to the origin of this model is contained in Reference 17.

Vorticity production at the walls only affects the diffusive transport terms. In this example we consider a control volume which is adjacent to the bottom surface of the cavity. We begin with the left-hand side of equation (27) and interchange the order of integration for the term which represents the diffusive flow across the surface y_1. Thus the total of the four diffusive terms become

$$\begin{aligned}
&Pr\int_t^{t+\Delta t}\left[\int_{y_1}^{y_2}\left(\frac{\partial\omega}{\partial x}(x_2, y, t) - \frac{\partial\omega}{\partial x}(x_1, y, t)\right)\mathrm{d}y + \int_{x_1}^{x_2}\frac{\partial\omega}{\partial y}(x, y_2, t)\,\mathrm{d}x\right]\mathrm{d}t \\
&\quad - \int_{x_1}^{x_2}\left(Pr\int_t^{t+\Delta t}\frac{\partial\omega}{\partial y}(x, 0, t)\mathrm{d}t\right)\mathrm{d}x \\
&= Pr\frac{\Delta t}{2}\frac{1}{576}[168(\omega^+ + \omega)_1 - 912(\omega^+ + \omega)_2 + 168(\omega^+ + \omega)_3 + 144(\omega^+ + \omega)_4 \\
&\quad + 288(\omega^+ + \omega)_5 + 144(\omega^+ + \omega)_6 - 24(\omega^+ + \omega)_7 + 48(\omega^+ + \omega)_8 - 24(\omega^+ + \omega)_9] \\
&\quad - \int_{x_1}^{x_2}\left(Pr\int_t^{t+\Delta t}\frac{\partial\omega}{\partial y}(x, 0, t)\mathrm{d}t\right)\mathrm{d}x.
\end{aligned} \tag{34}$$

In evaluating the integrals we have set $y_1 = 0$, $y_2 = h/2$, $x_1 = h/2$ and $x_2 = 3h/2$.

We next substitute (33) into the above equation and note that the normal to the surface is in the y-direction. Also the positive ambiguous sign in (33) is chosen since a positive 'slip' velocity produces negative free vorticity at the wall. Thus $\partial\omega/\partial y$, which represents the flux of this newly created vorticity, is positive at the wall.

The remaining transport terms must also be modified because of the changed limits of integration. The final equation is given by

$$\begin{aligned}
&\omega_1^+(8C_1 - 168C_2) + \omega_2^+(176C_1 + 912C_2) + \omega_3^+(8C_1 - 168C_2) + \omega_4^+(5C_1 - 144C_2) \\
&\quad + \omega_5^+(110C_1 - 288C_2) + \omega_6^+(5C_1 - 144C_2) + \omega_7^+(-C_1 + 24C_2) \\
&\quad + \omega_8^+(-22C_1 - 48C_2) + \omega_9^+(-C_1 + 24C_2) + \frac{\Delta t}{2}\Big[[\hat{\omega}^+](x_2)\dot{V}_{i,\omega}\Big(\frac{3h}{2}, t\Big) \\
&\quad - [\hat{\omega}^+](x_1)\dot{V}_{i,\omega}\Big(\frac{h}{2}, t\Big) + [\hat{\omega}^+](y_2)\dot{V}_{i,\omega}\Big(\frac{h}{2}, t\Big)\Big] \\
&= \omega_1(8C_1 + 1688C_2) + \omega_2(176C_1 - 912C_2) + \omega_3(8C_1 + 168C_2) \\
&\quad + \omega_4(5C_1 + 144C_2) + \omega_5(110C_1 + 288C_2) + \omega_6(5C_1 + 144C_2) \\
&\quad + \omega_7(-C_1 - 24C_2) + \omega_8(-22C_1 + 48C_2) + \omega_9(-C_1 - 24C_2) \\
&\quad - \frac{\Delta t}{2}\Big[[\hat{\omega}](x_2)\dot{V}_{i,\omega}\Big(\frac{3h}{2}, t\Big) - [\hat{\omega}](x_1)\dot{V}_{i,\omega}\Big(\frac{h}{2}, t\Big) + [\hat{\omega}](y_2)\dot{V}_{i,\omega}\Big(\frac{h}{2}, t\Big)\Big] \\
&\quad + RaPr\frac{\Delta t}{2}\frac{C_1}{h}[-96(\theta^+ + \theta)_1 + 96(\theta^+ + \theta)_3 - 60(\theta^+ + \theta)_4 \\
&\quad + 60(\theta^+ + \theta)_6 + 12(\theta^+ + \theta)_7 - 12(\theta^+ + \theta)_9] - \int_{x_1}^{x_2} U_{\text{slip}}(x, t)\mathrm{d}x, \qquad (35)
\end{aligned}$$

where

$$\int_{x_1}^{x_2} U_{\text{slip}}(x, t)\mathrm{d}x = \frac{h}{24}[U_{\text{slip}(i-1,\omega)} + 22U_{\text{slip}(i,\omega)} + U_{\text{slip}(i+1,\omega)}](t). \qquad (36)$$

Note that the values of C_1 and C_2 have been given previously.

Energy equation

For control volumes away from the cavity walls the evaluation of all the transport terms in the energy equation follows the procedure given above for the vorticity transport equation. However, at the cavity walls the boundary conditions are of a different form. The temperature values for node points on the left- and right-hand vertical walls are assigned the values $+0{\cdot}5$ and $-0{\cdot}5$ respectively. For the top and bottom surfaces there is no heat flow. Therefore the normal derivatives are zero there but the temperatures still need to be determined along these surfaces. The modification required for control volumes on the lower boundary, for example, parallels that given in equation (34). However, the last term is zero.

Evaluation of the velocity field

The horizontal components of velocity are evaluated at each point on the vertical surfaces of control volumes from equation (5). Only the distribution of vertical components of velocity along the horizontal midplane of the cavity is evaluated from equation (6) at the steady state condition.

Equation (6) is also used to evaluate the 'slip' velocities along the vertical walls of the cavity. In each case the numerical procedure is the same.

The velocity components are written as double finite sums of individual contributions as follows:

$$u(x, y, t) = \sum_{i=1}^{NX} \sum_{j=1}^{NY} \Delta u_{i,j}(x, y, t), \tag{37}$$

$$v(x, y, t) = \sum_{i=1}^{NX} \sum_{j=1}^{NY} \Delta v_{i,j}(x, y, t), \tag{38}$$

where NX and NY denote the number of control volumes in the horizontal and vertical directions. In this study $NX = NY = N$ since the cavity is square and the mesh is uniform. The terms $\Delta u_{i,j}$ and $\Delta v_{i,j}$ are the velocity components induced by the free vorticity in the control volume of cross-sectional area $\Delta A_{i,j}$. They can be expressed in exact form by

$$\Delta u_{i,j} = \iint_{\Delta A_{i,j}} K_{\mathrm{I}}(x, y, \xi, \eta)\, \omega(\xi, \eta, t)\, \mathrm{d}\xi\, \mathrm{d}\eta, \tag{39}$$

$$\Delta v_{i,j} = \iint_{\Delta A_{i,j}} K_{\mathrm{II}}(x, y, \xi, \eta)\, \omega(\xi, \eta, t)\, \mathrm{d}\xi\, \mathrm{d}\eta. \tag{40}$$

At this point we introduce the simplifying assumption that $\omega(\xi, \eta, t)$ is uniform over te area of the control volume. We take this to be the volume average of the vorticity, $\langle \omega(t) \rangle_{i,j}$, the expression for which is given by the right-hand side of equation (26) with the ' + ' omitted from the vorticity values. Then the vorticity can be factored out in front of the integrals in (39) and (40). Following this step, the integrations of (39) with respect to η and (40) with respect to ξ can be carried out exactly in closed form. The final results are in the form of an average vorticity multiplied by a coefficient which is only a function of the mesh geometry. That is,

$$u(x, y, t) = \sum_{i=1}^{NX} \sum_{j=1}^{NY} \langle \omega(t) \rangle_{i,j} CU_{i,j}(x, y) \tag{41}$$

$$v(x, y, t) = \sum_{i=1}^{NX} \sum_{j=1}^{NY} \langle \omega(t) \rangle_{i,j} CV_{i,j}(x, y), \tag{42}$$

where,

$$\begin{aligned} CU_{i,j} = \frac{1}{4\pi} \int_{\xi_1}^{\xi_2} \Bigg[& \ln \frac{\sin^2[(\pi/a)(x-\xi)] + \sinh^2[(\pi/a)(y-\eta_2)]}{\sin^2[(\pi/a)(x-\xi)] + \sinh^2[(\pi/a)(y-\eta_1)]} \\ & - \ln \frac{\sin^2[(\pi/a)(x+\xi)] + \sinh^2[(\pi/a)(y-\eta_2)]}{\sin^2[(\pi/a)(x+\xi)] + \sinh^2[(\pi/a)(y-\eta_1)]} - \ln \frac{\sin^2[(\pi/a)(x+\xi)] + \sinh^2[(\pi/a)(y+\eta_2)]}{\sin^2[(\pi/a)(x+\xi)] + \sinh^2[(\pi/a)(y+\eta_1)]} \\ & + \ln \frac{\sin^2[(\pi/a)(x-\xi)] + \sinh^2[(\pi/a)(y+\eta_2)]}{\sin^2[(\pi/a)(x-\xi)] + \sinh^2[(\pi/a)(y+\eta_1)]} - \sum_{n=1}^{\infty} \Bigg(\ln \frac{\sin^2[(\pi/a)(x+\xi)] + \sinh^2[(\pi/a)(y-2nH+\eta_2)]}{\sin^2[(\pi/a)(x+\xi)] + \sinh^2[(\pi/a)(y-2nH+\eta_1)]} \\ & + \ln \frac{\sin^2[(\pi/a)(x-\xi)] + \sinh^2[(\pi/a)(y-2nH+\eta_2)]}{\sin^2[(\pi/a)(x-\xi)] + \sinh^2[(\pi/a)(y-2nH+\eta_1)]} - \ln \frac{\sin^2[(\pi/a)(x-\xi)] + \sinh^2[(\pi/a)(y+2nH-\eta_2)]}{\sin^2[(\pi/a)(x-\xi)] + \sinh^2[(\pi/a)(y+2nH-\eta_1)]} \\ & + \ln \frac{\sin^2[(\pi/a)x+\xi)] + \sinh^2[(\pi/a)(y+2nH-\eta_2)]}{\sin^2[(\pi/a)x+\xi)] + \sinh^2[(\pi/a)(y+2nH-\eta_1)]} - \ln \frac{\sin^2[(\pi/a)(x-\xi)] + \sinh^2[(\pi/a)(y-2nH-\eta_2)]}{\sin^2[(\pi/a)(x-\xi)] + \sinh^2[(\pi/a)(y-2nH-\eta_1)]} \\ & + \ln \frac{\sin^2[(\pi/a)(x+\xi)] + \sinh^2[(\pi/a)(y-2nH-\eta_2)]}{\sin^2[(\pi/a)(x+\xi)] + \sinh^2[(\pi/a)(y-2nH-\eta_1)]} + \ln \frac{\sin^2[(\pi/a)(x+\xi)] + \sinh^2[(\pi/a)(y+2nH+\eta_2)]}{\sin^2[(\pi/a)(x+\xi)] + \sinh^2[(\pi/a)(y+2nH+\eta_1)]} \\ & - \ln \frac{\sin^2[(\pi/a)(x-\xi)] + \sinh^2[(\pi/a)(y+2nH+\eta_2)]}{\sin^2[(\pi/a)x-\xi)] + \sinh^2[(\pi/a)(y+2nH+\eta_1)]} \Bigg) \Bigg] \mathrm{d}\xi, \end{aligned} \tag{43}$$

$$CV_{i,j} = \frac{1}{4\pi}\int_{\eta_1}^{\eta_2}\left[\ln\frac{\sin^2[(\pi/a)(x+\xi_2)]+\sinh^2[(\pi/a)(y-\eta)]}{\sin^2[(\pi/a)(x+\xi_1)]+\sinh^2[(\pi/a)(y-\eta)]}\right.$$
$$+\ln\frac{\sin^2[(\pi/a)(x-\xi_2)]+\sinh^2[(\pi/a)(y-\eta)]}{\sin^2[(\pi/a)(x-\xi_1)]+\sinh^2[(\pi/a)(y-\eta)]}-\ln\frac{\sin^2[(\pi/a)(x-\xi_2)]+\sinh^2[(\pi/a)(y+\eta)]}{\sin^2[(\pi/a)(x-\xi_1)]+\sinh^2[(\pi/a)(y+\eta)]}$$
$$-\ln\frac{\sin^2[(\pi/a)(x+\xi_2)]+\sinh^2[(\pi/a)(y+\eta)]}{\sin^2[(\pi/a)(x+\xi_1)]+\sinh^2[(\pi/a)(y+\eta)]}-\sum_{n=1}^{\infty}\left(-\ln\frac{\sin^2[(\pi/a)(x-\xi_2)]+\sinh^2[(\pi/a)(y-2nH+\eta)]}{\sin^2[(\pi/a)(x-\xi_1)]+\sinh^2[(\pi/a)(y-2nH+\eta)]}\right.$$
$$-\ln\frac{\sin^2[(\pi/a)(x+\xi_2)]+\sinh^2[(\pi/a)(y-2nH+\eta)]}{\sin^2[(\pi/a)x+\xi_1)]+\sinh^2[(\pi/a)(y-2nH+\eta)]}+\ln\frac{\sin^2[(\pi/a)(x+\xi_2)]+\sinh^2[(\pi/a)(y+2nH-\eta)]}{\sin^2[(\pi/a)(x+\xi_1)]+\sinh^2[(\pi/a)(y+2nH-\eta)]}$$
$$+\ln\frac{\sin^2[(\pi/a)x-\xi_2)]+\sinh^2[(\pi/a)(y+2nH-\eta)]}{\sin^2[(\pi/a)x-\xi_1)]+\sinh^2[(\pi/a)(y+2nH-\eta)]}-\ln\frac{\sin^2[(\pi/a)(x+\xi_2)]+\sinh^2[(\pi/a)(y-2nH+\eta)]}{\sin^2[(\pi/a)(x+\xi_1)]+\sinh^2[(\pi/a)(y-2nH+\eta)]}$$
$$+\ln\frac{\sin^2[(\pi/a)(x-\xi_2)]+\sinh^2[(\pi/a)(y-2nH+\eta)]}{\sin^2[(\pi/a)(x-\xi_1)]+\sinh^2[(\pi/a)(y-2nH+\eta_1)]}-\ln\frac{\sin^2[(\pi/a)(x+\xi_2)]+\sinh^2[(\pi/a)y+2nH-\eta)]}{\sin^2[(\pi/a)(x+\xi_1)]+\sinh^2[(\pi/a)y+2nH-\eta)]}$$
$$\left.\left.-\ln\frac{\sin^2[(\pi/a)(x-\xi_2)]+\sinh^2[(\pi/a)(y+2nH-\eta)]}{\sin^2[(\pi/a)(x-\xi_1)]+\sinh^2[(\pi/a)(y+2nH-\eta)]}\right)\right]d\eta. \tag{44}$$

The final integrations with respect to ξ and η are carried out numerically using an eight-point Gauss quadrature formula. In practice it is found that the series can be truncated beyond $n = 8$. This is sufficient to fix the velocity to within 12 significant figures.

Nusselt number

The Nusselt number expressions given by equations (12) and (13) are evaluated only after a steady state solution has been attained. The biquadratic interpolation formulae are used to represent θ over the domain. Values of θ and $\partial\theta/\partial x$ are next evaluated at the volume points of the mesh. Values for u are also needed at these points and are computed from (41). A quadratic formula is used to interpolate these values between volume points. When these expressions are substituted into (12) and (13) and the integrations are carried out, it is equivalent to using a central difference formula for $\partial\theta/\partial x$ and Simpson's rule for the integrations.

Two other results are of interest. These are the maximum and minimum values of the Nusselt number along the left-hand vertical wall of the cavity (i.e. at $x = 0$). To find these, the four adjacent points to that at which the extreme values of Nu occur are identified. Then a fourth-degree polynomial is passed through the five points. This polynomial is then differentiated and set equal to zero. The values of y at which the slopes vanish are next determined by solving the cubic equation numerically using the secant method. These values of y are finally substituted into the polynomial in order to find the values of the extrema. This is the same procedure used in Reference 2.

Conservation law for total vorticity

The integral law for the conservation of total vorticity is given in equation (16). It has been specialized to two-dimensional flow in a square cavity. For the numerical evaluation of this equation we substitute the vorticity production model, equation (33), for the flux terms given by $\partial\omega/\partial x$ or $\partial\omega/\partial y$.

In order to interpret the ambiguous sign in (33), we invoke the 'right-hand rule'. With the palm resting on the solid surface, the fingers of the right hand point in the direction of the 'slip' velocity, and the thumb points in the direction of the vorticity created by the (apparent) slip velocity. The created vorticity is considered to be positive if it points out of the plane of the flow. For positive vorticity production, $\partial\omega/\partial n$ is negative, and vice versa. Here n denotes the normal direction drawn from the wall inwards towards the cavity. We now denote the slip velocity on the

horizontal and vertical walls respectively by u_{slip} and v_{slip}. Thus we obtain from (33) for suitably small Δt,

$$Pr\frac{\partial\omega}{\partial x}(0, y, t) \simeq -\frac{v_{slip}(0, y, t)}{\Delta t}, \tag{45a}$$

$$Pr\frac{\partial\omega}{\partial x}(1, y, t) \simeq -\frac{v_{slip}(1, y, t)}{\Delta t}, \tag{45b}$$

$$Pr\frac{\partial\omega}{\partial y}(x, 0, t) \simeq +\frac{u_{slip}(x, 0, t)}{\Delta t}, \tag{45c}$$

$$Pr\frac{\partial\omega}{\partial y}(x, 1, t) \simeq +\frac{u_{slip}(x, 1, t)}{\Delta t}. \tag{45d}$$

Once these expressions are introduced into equation (16), one obtains

$$0 = RaPr - \int_0^1 \frac{v_{slip}(0, y, t)}{\Delta t}dy + \int_0^1 \frac{v_{slip}(1, y, t)}{\Delta t}dy + \int_0^1 \frac{u_{slip}(x, 0, t)}{\Delta t}dx - \int_0^1 \frac{u_{slip}(x, 1, t)}{\Delta t}dx. \tag{46}$$

The numerical integrations are carried out using Simpson's rule. Special note is made of the fact that the mesh has quarter-size control volumes at the four corners of the cavity (see Figure 2). Therefore these regions are handled in a special way. The slip velocities are identically zero at the four corner points of the cavity. This is a consequence of the image system which has been adopted for the vorticity field. The slip velocities nearest the corners are evaluated at distances $h/4$ away from the corners on each of the surfaces. The remaining slip velocities are evaluated midway between mesh lines.

Choice of spatial and time increments

The numerical calculations are carried out using different meshes, time increments and choices of the Rayleigh number. However, we hold Pr fixed at a value of 0·71.

It is reasonable to expect that the choice of the time and spatial increments should be dictated in part by the Rayleigh number. In fact, the form of the governing equations for the scaled velocity and vorticity variables, given previously as equations (17)–(19), suggests that this is the case.

Without regard to the specific discrete version of these equations, we simply examine the denominators of the equations and deduce from (17) that

$$O[(Ra)^{1/2}\Delta x] = O[(Ra)^{1/2}\Delta y]. \tag{47}$$

In a similar manner, from (18) and (19) we have

$$O[Ra\Delta t] = O[(Ra)^{1/2}\Delta x] = O[(Ra)^{1/2}\Delta y] = O[Ra(\Delta x)^2] = O[Ra(\Delta y)^2]. \tag{48}$$

Since $Pr = O(1)$ we do not need to include this parameter in our estimates.

Besides the obvious conclusion that Δx and Δy are the same order of magnitude, we see that $O[(Ra)^{1/2}\Delta x] = O[Ra(\Delta x)^2]$. Thus the latter two quantities must each be of order unity. This leads to the conclusion that

$$\Delta x = O\left(\frac{1}{(Ra)^{1/2}}\right). \tag{49}$$

It also follows that

$$\Delta t = O\left(\frac{1}{Ra}\right) = O(\Delta x^2). \tag{50}$$

We will demonstrate by actual numerical experiment that these order-of-magnitude estimates are quite reliable.

Computational procedure

We conclude with a description of the computational procedure used to solve the equations in this section. All flow variables (velocity, vorticity and temperature) are initially zero. The temperatures of the hot and cold surfaces are changed spontaneously to their prescribed values and the energy equation is solved for the temperature throughout the fluid. During this stage of the calculation there is no convective transport of energy because the velocity variables are held fixed at zero. This temperature distribution is next used in the vorticity transport equation and the vorticity is found throughout the fluid, also in the absence of convection. There is no vorticity production at the walls during this first phase of the calculation. This is because $t = 0$ in equation (33) and the slip velocity is initially zero. Now that a vorticity field has been established, the x-component of velocity can be calculated from equation (41) and the vertical velocity components evaluated from the continuity equation. The last step is to calculate the 'slip' velocities on the boundary of the cavity. For the horizontal planes, (41) is used with $y = 0$ and 1. For the vertical boundaries, (42) is used with $x = 0$ and 1. These 'slip' velocities are used to determine the vorticity production at the walls during the next phase of the calculation.

This completes one cycle of the calculation and the solution is now known at time level Δt. The procedure continues with the solution of the energy equation followed by the solution of the vorticity transport equation. During this phase of the calculation there is convective transport of energy and total vorticity and there is also vorticity production at the walls, as mentioned above. The last step is to determine the velocity field and the new 'slip' velocities at the boundaries, which quantities are used to advance the solution in the next phase of the calculation, and so on.

RESULTS AND DISCUSSION

Calculations have been carried out for three different Rayleigh numbers. These are $Ra = 10^3$, 10^4 and 10^5. Different meshes and time increments were also used. We make no claim here that the results are the best that one can achieve. In that sense these are not the 'answers to the problem'. However, we will demonstrate that the finite volume algorithm with adaptive upwind convection produces very accurate results in the steady state, even on relatively coarse meshes.

We use the bench-mark solution from Reference 2 to assess the accuracy of our steady state predictions. The bench-mark solution was obtained using a finite difference scheme which incorporates forward time and centred space derivatives. The method of false transients was employed in a vorticity–stream function formulation. In contrast, our results were obtained using a 'time-accurate' scheme and the vorticity–velocity formulation was used. This is not an efficient algorithm to use if one is only interested in a steady state solution. However, our main intent is to present transient results and these will be presented and discussed presently.

Several numerical experiments have been performed in order to test the temporal convergence of the method as well as the utility of the order-of-magnitude estimates made for the time and spatial increments. These are given by equations (49) and (50). The results of the numerical experiments are presented in the next section.

Numerical experiments

We first examine the effect of the time increment on the steady state solutions. We do this using 11×11 and 21×21 meshes for $Ra = 10^3$. These calculations can be performed relatively cheaply and the findings can be generalized to other meshes and values of Ra.

It can be argued that if the transient scheme is stable and the solutions converge to a steady state, then the final solution should be independent of the time increment used. However, this will not necessarily be the case. Indeed, schemes which do produce different steady state solutions for different time increments can still be useful and cost-effective, even for steady flow simulations.[21]

The effect of the time increment on the steady state results is illustrated in Figure 5. The predictions are shown for the scaled maximum velocities in the horizontal and vertical directions and the average Nusselt number. The results for the 11×11 mesh ($h = \Delta x = \Delta y = 0{\cdot}1$) are represented by the circles. Five choices of the ratio $\Delta t/\Delta x^2$ were used. These are 0·1, 0·2, 0·3, 0·35 and 0·4. For the 21×21 mesh ($h = 0{\cdot}05$) the results are shown by the squares. Two values of $\Delta t/\Delta x^2$ were used, namely 0·1 and 0·3. The bench-mark results are shown by the horizontal lines.

It can be seen that the solution improves as the time increment is reduced. There is, in fact, first-order convergence in time. Note that extrapolation to a zero time increment does not produce the bench-mark result, but this is not surprising since the mesh is still relatively coarse. Clearly, the results for $h = 0{\cdot}05$ are quite good for both choices of the time increment. That is, the results for the finer mesh show a weaker dependence on Δt than do those for the coarser mesh. It is expected that as the mesh is refined further there will be almost no dependence of the steady state solution on Δt provided $\Delta t/\Delta x^2 = O(1)$.

The reason that Δt affects the steady state solution can be traced to the numerical boundary condition, equation (33), imposed on the vorticity transport equation. For accurate simulations the time increment should be of the order of the diffusion time corresponding to the spatial increment near the wall.[17] That is precisely the criterion given by equation (50).

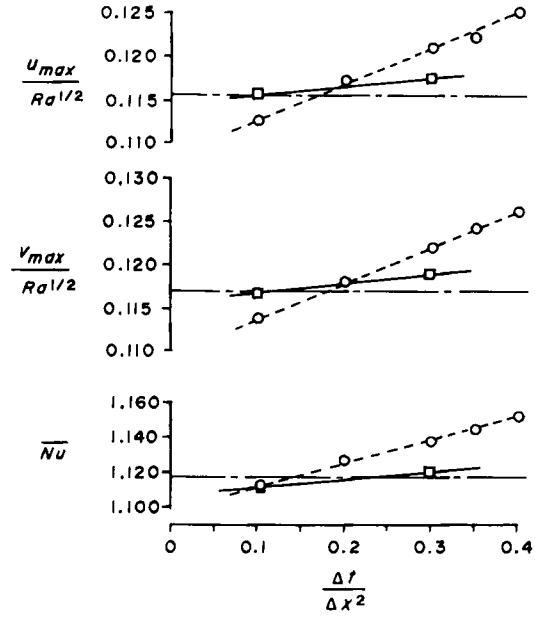

Figure 5. Effect of time increment on convergence of steady state solution for two mesh sizes --○--, $h = 0{\cdot}1$; —□—, $h = 0{\cdot}05$; ———, bench-mark solution

The fact that the error in the solution shows a first-order dependence on Δt is believed to be caused by the mixed-time-level treatment of the convective transport terms. The use of the trapezoidal rule for the time integration of the diffusion and buoyancy terms has a truncation error $O(\Delta t^3)$. We cannot estimate the truncation error for the convective terms because of the mixed-time-level scheme used. However, the results of Figure 5 suggest that it is close to $O(\Delta t)$ since this is the overall accuracy of the time integration scheme.

Another test of the results is provided by the conservation law for total vorticity. This has not been examined previosly for this problem but has been used in other test problems.[8] The form of the conservation law which is used here, and which is consistent with the Boussinesq approximation, is given by equation (46). This law states that the net dimensionless vorticity produced at all the solid boundaries must equal the $RaPr$ product. The relative error can thus be found by dividing the right-hand side of (46) by this product and comparing the total term with zero. In these calculations $RaPr = 710$.

The degree to which the conservation law for total vorticity is satisfied is shown in Figure 6. The error is expressed as a percentage and the symbols are the same as those used in Figure 5. It is clear that for either mesh the conservation law will be satisfied exactly as $\Delta t \to 0$. Also the results for the finer mesh are only slightly better than those for the coarser mesh.

From these tests we concludce that a good time step criterion is $\Delta t/\Delta x^2 = 0{\cdot}1$. We view this as slightly conservative, but the accuracy of the steady state results is entirely satisfactory when this criterion is used and we expect the accuracy of the transient solutions to be likewise satisfactory.

Before turning to the transient results, it cannot escape notice that the steady state results shown in Figure 5 for $h = 0{\cdot}05$ and $\Delta t/\Delta x^2 = 0{\cdot}1$ are essentially indistinguishable from the benchmark solution for this small value of $Ra = 10^3$. This should not be too surprising since in this case $\Delta x(Ra)^{1/2} = 1{\cdot}58$. Thus the criterion given by equation (49) is essentially satisfied. This allows one to assess the relative coarseness of the mesh and we conclude that an 11×11 mesh is quite adequate for this small Rayleigh number.

Transient results

In what follows, a 21×21 mesh has been used exclusively and $\Delta t/\Delta x^2 = 0{\cdot}1$. Also the velocity and vorticity variables have all been scaled by dividing these quantities by $Ra^{1/2}$.

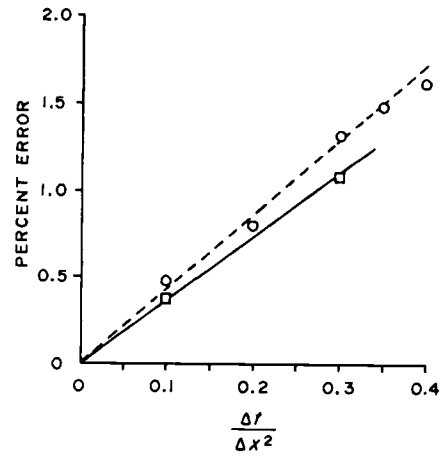

Figure 6. Effect of time increment on the error in the global conservation of total vorticity; --○--, $h = 0{\cdot}1$; —□—, $h = 0{\cdot}05$

We first demonstrate the approach to the steady state by showing the time variation of the vorticity at the centre of the cavity. The results for the three different values of Ra are shown in Figure 7. The calculations were ceased after the curves followed a horizontal asymptote for an appreciable length of time. It appears that the choice of the scaling factor (i.e. $Ra^{1/2}$) is entirely appropriate for determining the order of magnitude of the vorticity.

The study by Gresho *et al.*[16], which became known to the authors after the present work was completed, presents some transient results for this problem but for slightly different physical parameters, namely $Pr = 1{\cdot}0$ and $Ra = 10^5$. Whereas a direct comparison of results is not possible, the qualitative features of their temperature and our vorticity results are very similar. They plot the transient development of the temperature at a point on the midplane and three-quarters of the distance between the heated and cooled walls. The 'valley-to-peak' nature of the two curves is the same. Also their results show steady state behaviour after $t \simeq 0{\cdot}15$ whereas ours show this after $t \simeq 0{\cdot}10$.

In the remainder of this section we present distributions of vorticity, temperature and velocity along different planes in the cavity and at different times. These are shown for the two extreme values of the Rayleigh modulus, namely $Ra = 10^3$ and 10^5.

The distribution of vorticity across the horizontal midplane of the cavity is shown in Figures 8 and 9 for the three different Rayleigh numbers and several time levels. Recall that the enforcement of the viscous adherence condition on the two vertical walls causes positive vorticity to be produced there. Moreover, the temperature gradient in the horizontal direction gives rise to a volumetric source of vorticity within the fluid.

A negative temperature gradient produces negative vorticity, and vice versa. Since this gradient is negative in the thermal layers next to the heated and cooled vertical walls, it is not surprising that the negative vorticity produced by it eventually overwhelms the positive vorticity created at the walls, thus driving the fluid vorticity to negative values in these layers. However, for the larger Rayleigh number the vorticity increases again in the central part of the cavity. This is consistent

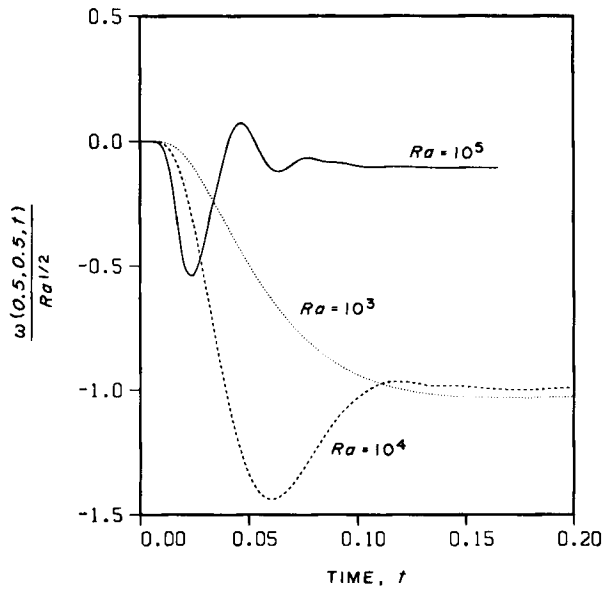

Figure 7. Time variation of the scaled vorticity at the midpoint of the cavity

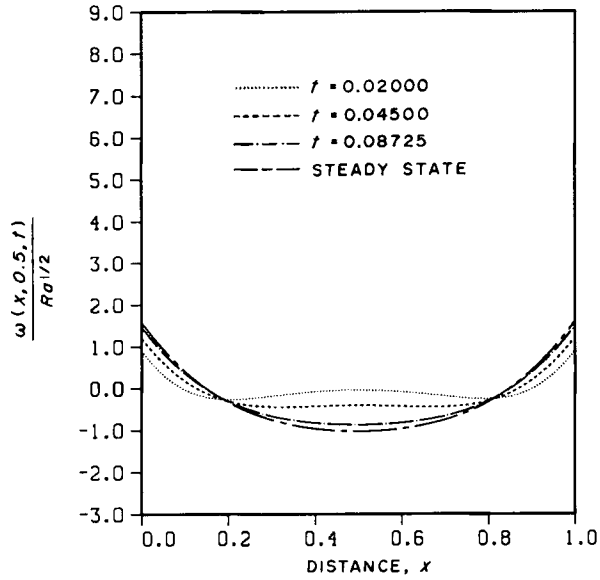

Figure 8. Distribution of scaled vorticity along the horizontal midplane of the cavity at several time levels, $h = 0{\cdot}05$ and $Ra = 10^3$

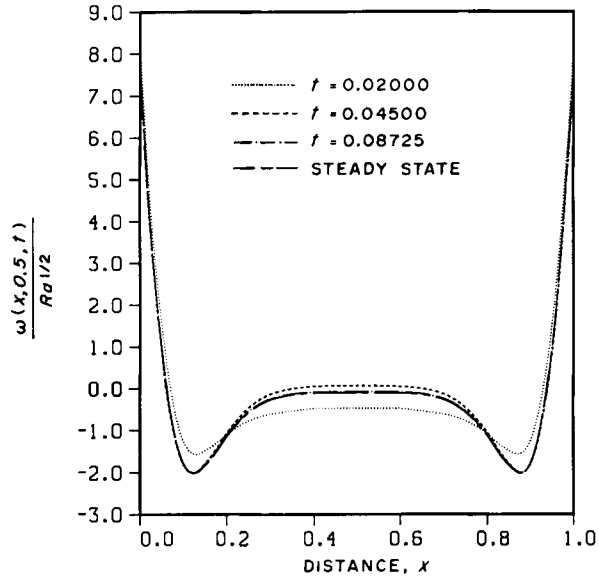

Figure 9. Distribution of scaled vorticity along the horizontal midplane of the cavity at several time levels, $h = 0{\cdot}05$ and $Ra = 10^5$

with the shape of the corresponding temperature profiles for this horizontal midplane. These are shown in Figures 10 and 11. For $Ra = 10^5$ the temperature gradient in the x-direction is positive during a substantial part of the transient development of the flow. This is sufficiently strong to cause the vorticity at the central point of the cavity to reach a momentary positive peak value at $t \simeq 0{\cdot}05$, as shown in Figure 7.

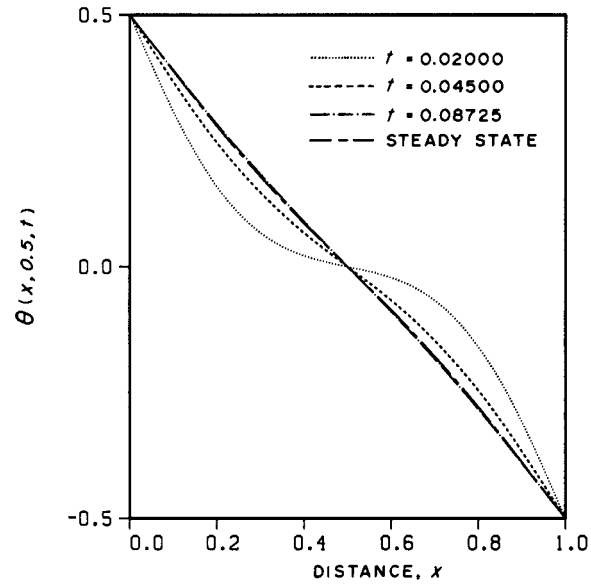

Figure 10. Distribution of temperature along the horizontal midplane of the cavity at several time levels, $h = 0{\cdot}05$ and $Ra = 10^3$

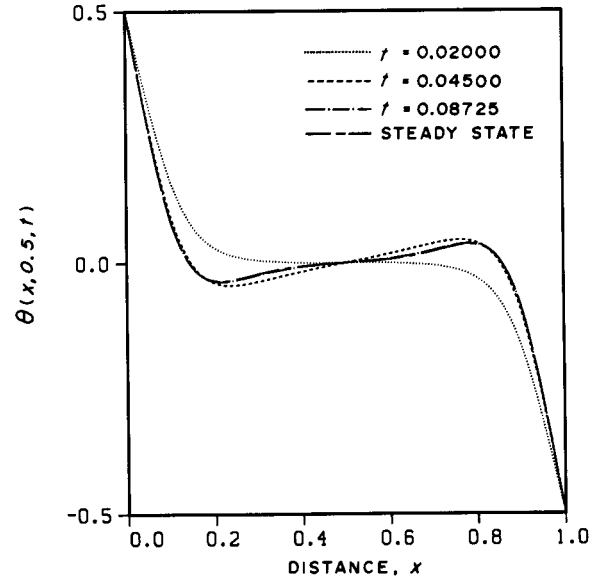

Figure 11. Distribution of temperature along the horizontal midplane of the cavity at several time levels, $h = 0{\cdot}05$ and $Ra = 10^5$

The transient development of the horizontal component of velocity is depicted in Figures 12 and 13. These profiles correspond to $x = 0{\cdot}525$ and not to the vertical midplane itself. This is a location which coincides with one of the mesh lines closest to the centre plane and it is only along these lines that the velocity is actually calculated. We could have chosen $x = 0{\cdot}475$, but the two profiles are indistinguishable by eye.

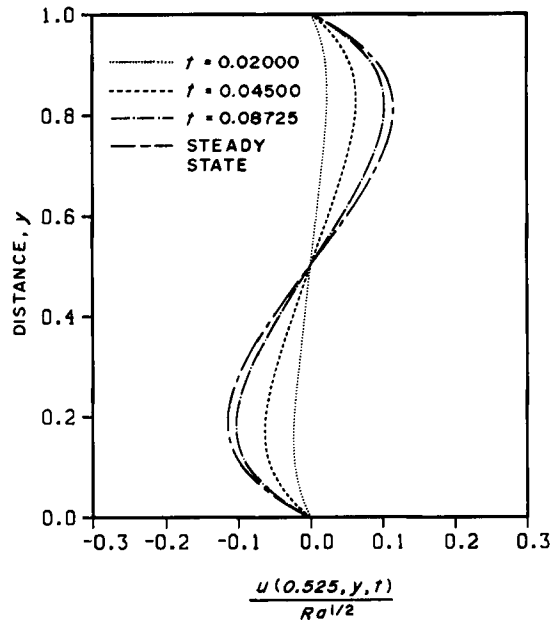

Figure 12. Distribution of scaled horizontal velocity component near the vertical midplane of the cavity at several time levels, $h = 0{\cdot}05$ and $Ra = 10^3$

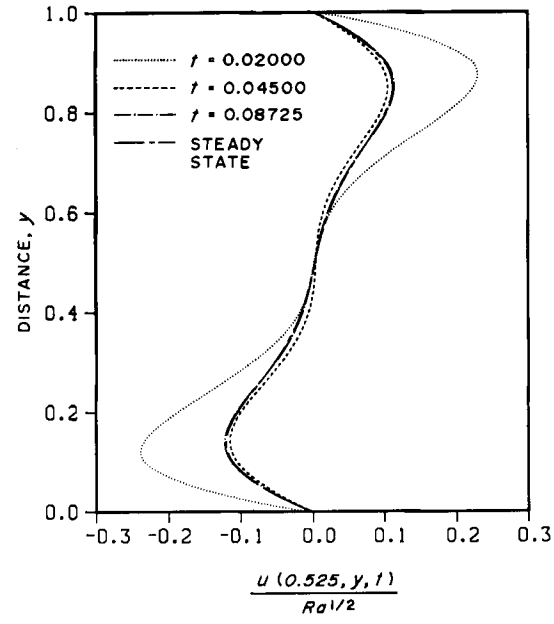

Figure 13. Distribution of scaled horizontal velocity component near the vertical midplane of the cavity at several time levels, $h = 0{\cdot}05$ and $Ra = 10^5$

In viewing all of these profiles it appears that 21 points are sufficient to define the curves for the smaller Rayleigh number. However, for $Ra = 10^5$ more points should be used, or at least more points should be concentrated near the wall layers. For the largest value of Ra, $\Delta x(Ra)^{1/2} = 15{\cdot}8$, which is no longer of order unity. Therefore we should suspect that the mesh is too coarse to resolve the fine details of the flow at this Rayleigh number. For $Ra = 10^4$ this parameteris 5·0, which is more reasonable. Nevertheless, the mesh is probably only marginally adequate for this Rayleigh number.

Steady state results

Besides the bench-mark solution, de Vahl Davis[2] presents tabulated results for several meshes and a range of Rayleigh numbers. Therefore we can compare our steady state results with those obtained by his method on the same mesh. We have used 11 × 11 and 21 × 21 meshes for the three choices of Rayleigh number given previously. These results are presented in Tables I–III.

Table I. Steady state results for $Ra = 10^3$

	Present work (11 × 11)	de Vahl Davis (11 × 11)	Bench-mark	Present work (21 × 21)	de Vahl Davis (21 × 21)
$u_{max}/Ra^{1/2}$	0·1126	0·1084	0·1154	0·1154	0·1135
y	0·810	0·801	0·813	0·813	0·811
$v_{max}/Ra^{1/2}$	0·1136	0·1091	0·1169	0·1167	0·1147
x	0·183	0·193	0·178	0·179	0·181
$\overline{Nu}$	1·114	1·096	1·118	1·113	1·111
$Nu_{1/2}$	1·119	1·104	1·118	1·118	1·114
Nu_0	1·111	1·105	1·117	1·109	1·113
Nu_{max}	1·497	1·462	1·505	1·479	1·491
y	0·099	0·141	0·092	0·097	0·112
Nu_{min}	0·693	0·723	0·692	0·715	0·702
y	1·000	0·936	1·000	1·000	1·000

Table II. Steady state results for $Ra = 10^4$

	Present work (11 × 11)	de Vahl Davis (11 × 11)	Bench-mark	Present work (21 × 21)	de Vahl Davis (21 × 21)
$u_{max}/Ra^{1/2}$	0·16584	0·16243	0·16178	0·16252	0·16189
y	0·817	0·808	0·823	0·822	0·820
$v_{max}/Ra^{1/2}$	0·19096	0·18055	0·19617	0·19606	0·19197
x	0·126	0·139	0·119	0·120	0·125
$\overline{Nu}$	2·294	2·171	2·243	2·248	2·212
$Nu_{1/2}$	2·290	2·170	2·243	2·243	2·213
Nu_0	2·252	2·307	2·238	2·310	2·255
Nu_{max}	3·562	3·637	3·528	3·680	3·603
y	0·155	0·211	0·143	0·143	0·165
Nu_{min}	0·567	0·676	0·586	0·594	0·610
y	1·000	1·000	1·000	1·000	1·000

Table III. Steady state results for $Ra = 10^5$

	Present work (11 × 11)	de Vahl Davis (11 × 11)	Bench-mark	Present work (21 × 21)	de Vahl Davis (21 × 21)
$u_{max}/Ra^{1/2}$	0·0962	0·1293	0·1098	0·1159	0·1153
y	0·844	0·846	0·855	0·855	0·854
$v_{max}/Ra^{1/2}$	0·1889	0·1888	0·2169	0·2124	0·1986
x	0·071	0·083	0·066	0·069	0·075
$\overline{Nu}$	4·369	4·446	4·519	4·576	4·454
$Nu_{1/2}$	4·300	4·381	4·519	4·559	4·455
Nu_0	4·594	4·767	4·509	4·522	4·716
Nu_{max}	7·449	6·538	7·717	7·678	7·901
y	0·048	0·218	0·081	0·095	0·133
Nu_{min}	0·719	1·516	0·729	0·710	0·797
y	1·000	1·000	1·000	0·973	1·000

For the sake of brevity in our discussion we will refer to the results obtained from Reference 2 simply as 'dVD'.

The quantities u_{max} and v_{max} are obtained from the velocity profiles along $x = 0{\cdot}5$ and $y = 0{\cdot}5$ respectively. The values of Nu_{max} and Nu_{min} are found along $x = 0$. Referring to Table I, which corresponds to $Ra = 10^3$, one sees that both sets of results for the 11 × 11 mesh are quite good. However, those obtained in the present study are marginally superior. There is a slight but still noticeable improvement when the mesh is refined to 21 × 21. In that instance the present predictions are in the most part indistinguishable from the bench-mark solution. There is only a slight discrepancy in the results for Nu_0, Nu_{max} and Nu_{min}. Since these are already witin 2% of the bench-mark values, the agreement is deemed to be satisfactory.

One would expect the accuracy of the predictions to deteriorate as the Rayleigh number is increased while keeping the mesh unchanged. This is not the case for the results obtained in the present study and shown in Table II. We see that for the finer mesh the results are still in remarkably good agreement with the bench-mark solution. Those of dVD are also quite satisfactory. However, we still believe that ours have a slight edge.

We remarked earlier that the physics of the problem dictates that the values of $\overline{Nu}$, $Nu_{1/2}$ and Nu_0 be the same. However, discretization errors will cause these to differ. Only Nu_0 shows an appreciable departure from the other two values. This is also true of the dVD results as well as the bench-mark solution. As pointed out by dVD, this is because the approximation used to calculate $\partial\theta/\partial x$ at $x = 0$ is formally less accurate (by a factor of two) than the central difference approximation used away from the wall. We will return to a further discussion of these heat transfer results subsequently.

The final tabulation of results for $Ra = 10^5$ is shown in Table III. Now it seems clear that the coarser mesh is inadequate for this case. Still, the present predictions seem slightly better than those of dVD. This is especially true of the Nusselt numbers. This same trend is found in the results for the finer mesh as well.

We conclude this section by showing the variation of the Nusselt number across the cavity, as given by equation (12). This is shown in Figures 14–16 for the three values of the Rayleigh number. The horizontal dashed line is the computed value of $\overline{Nu}$ and only the results for the 21 × 21 mesh are shown. Note that the scale on the abscissa is greatly expanded. In the absence of discretization errors, Nu_x should be uniform and equal to $\overline{Nu}$.

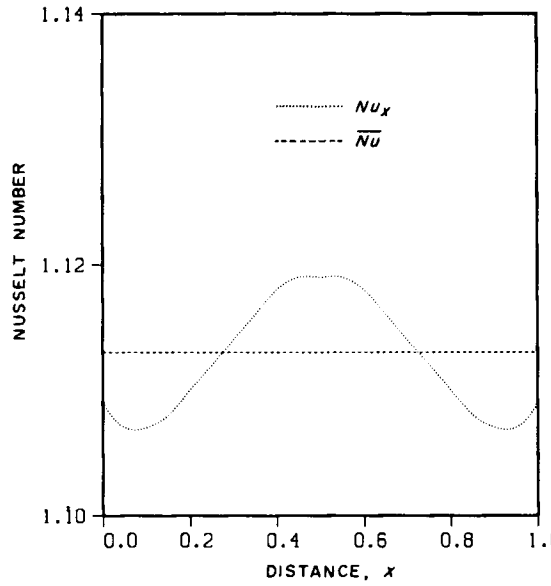

Figure 14. Comparison between the local and average Nusselt numbers in the cavity at steady state, $h = 0{\cdot}05$ and $Ra = 10^3$

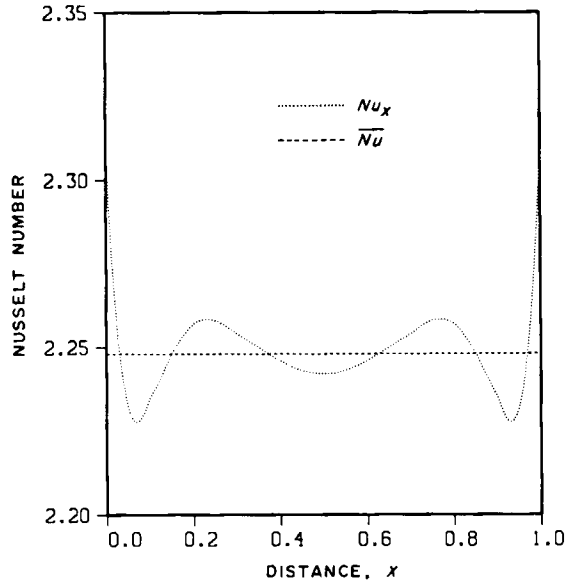

Figure 15. Comparison between the local and average Nusselt numbers in the cavity at steady state, $h = 0{\cdot}05$ and $Ra = 10^4$

For $Ra = 10^3$ the variation from wall to centreline is less than 1% of the mean value. It is slightly greater than this for $Ra = 10^4$. For $Ra = 10^5$ the variation is of the order of 2%. This is considered to be remarkably good, especially since it is clear that a 21 × 21 mesh has difficulty resolving the sharp peaks and valleys evident in the distribution shown in Figure 16.

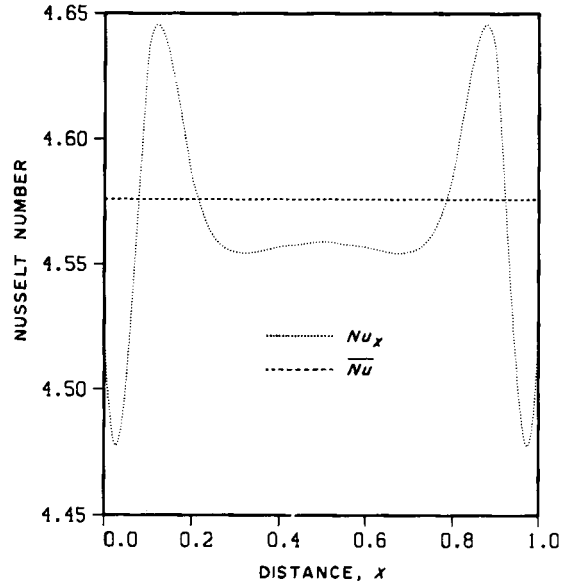

Figure 16. Comparison between the local and average Nusselt numbers in the cavity at steady state, $h = 0{\cdot}05$ and $Ra = 10^5$

CONCLUDING REMARKS

The new finite volume (FV) approach has been applied to an unsteady viscous flow problem with a substantial amount of complexities. The numerical predictions have been found to be quite good when compared with those obtained from Reference 2. In that study a finite difference (FD) scheme was used which incorporated second-order central differences for all space derivatives. Those FD solutions were then extrapolated to zero mesh size to obtain a numerical bench-mark solution. The predictions obtained with the present method were noticeably closer to the bench-mark solution than those obtained with the FD scheme on the same mesh. This shows that our FV scheme does have merit and in fact has a spatial convergence rate comparable to the FD scheme. This is significant because it does make use of an upwind treatment of the convection terms.

We have presented rational criteria for choosing time and spatial increments for the free convection problem which are independent of the particular discrete approximations used. According to these criteria, the time increment must be proportional to the diffusion time for the mesh, and the spatial increment must be proportional to the vorticity boundary layer thickness near the solid surfaces. This thickness is essentially the same as that for the thermal layer when the Prandtl number is near unity. Such was the case for the problem examined in the present study. This ensures that the regions of steep gradients can be resolved by the mesh. We strongly advocate that these criteria be observed, regardless of the numerical algorithm used, if physically meaningful solutions are to be obtained.

It is our conclusion that the present FV method continues to show great promise. However, it is very evident that it is considerably more complex than the FD scheme used by de Vahl Davis.[2] This introduces additional programming difficulties and increased central memory requirements. It would be premature to state categorically that this added expense is justified. Further testing

needs to be done before the full extent of the advantages and disadvantages of the present method can be known.

REFERENCES

1. R. B. Kinney and H. S. Mahdi, 'A new finite-volume approach with adaptive upwind convection', *Int. j. numer. methods eng.*, **26,** 1325–1343 (1988).
2. G. de Vahl Davis, 'Natural convection of air in a square cavity: a bench mark numerical solution', *Int. j. numer. methods fluids*, **3,** 249–264 (1983).
3. S. V. Patankar, *Numerical Heat Transfer and Fluid Flow*, McGraw-Hill, New York, 1980, Chap. 3.
4. R. W. MacCormack and R. F. Warming, 'Survey of computational methods for three-dimensional supersonic inviscid flows with shocks', *Advances in Numerical Fluid Dynamics, AGARD LS64*, 1973.
5. A. J. Baker, *Finite Element Computational Fluid Mechanics*, McGraw-Hill, New York, 1980, Chap. 4.
6. G. D. Raithby and K. E. Torrance, 'Upstream-weighted differencing schemes and their application to elliptic problems involving fluid flow', *Comput. Fluids*, **2,** 191–206 (1974).
7. G. de Vahl Davis and G. D. Mallinson, 'An evaluation of upwind and central difference approximations by a study of recirculating flow', *Comput. Fluids*, **4,** 29–43 (1976).
8. A. Benjamin and V. Denny, 'On the convergence of numerical solutions for 2-D flows in a cavity at large *Re*', *J. Comput. Phys.*, **33,** 340–358 (1979).
9. P. M. Gresho and R. L. Lee, 'Don't suppress the wiggles—they're telling you something', *Comput. Fluids*, **9,** 223–253 (1981).
10. A. Borthwick, 'Comparison between two finite-difference schemes for computing the flow around a cylinder', *Int. j. numer. methods fluids*, **6,** 275–290 (1986).
11. A. Jameson and D. A. Caughey, 'A finite volume method for transonic potential flow calculations', *AIAA 3rd Computational Fluid Dynamics Conf. No. 77–635*, Albuquerque, NM, 1977.
12. G. de Vahl Davis and I. P. Jones, 'Natural convection in a square cavity: a comparison exercise', *Int. j. numer. methods fluids*, **3,** 249–264 (1983).
13. T. N. Phillips, 'Natural convection in an enclosed cavity', *J. Comput. Phys.*, **54,** 365–381 (1984).
14. P. Luchini, 'An adaptive-mesh finite-difference solution method for the Navier–Stokes equations', *J. Comput. Phys.*, **68,** 283–306 (1987).
15. K. Küblbeck, G. P. Merker and J. Straub, 'Advanced numerical computation of two-dimensional time-dependent free convection in cavities', *Int. J. Heat Mass Transfer*, **23,** 203–217 (1980).
16. P. M. Gresho, R. L. Lee, S. T. Chan and R. L. Sani, 'Solution of time-dependent incompressible Navier–Stokes and Boussinesq equations using the Galerkin finite element method', *Approximate Methods for Navier–Stokes Problems, Lecture Notes in Mathematics, No. 771*, Springer-Verlag, New York, 1980, pp. 203–223.
17. S. C. Hung and R. B. Kinney, 'Unsteady viscous flow over a grooved wall: a comparison of two numerical methods', *Int. j. numer. methods fluids*, **8,** 1403–1437 (1988).
18. B. Gebhart, *Heat Transfer*, 2nd edn, McGraw-Hill, New York, 1971, Chap. 8.
19. M. J. Lighthill, 'Introduction. Boundary layer theory', in L. Rosenhead (ed.), *Laminar Boundary Layers*, Oxford University Press, 1963, pp. 57–60.
20. H. S. Mahdi, 'Analysis of unsteady heat transfer by natural convection in a two-dimensional square cavity using a high order finite-volume method', *Ph.D. Dissertation*, University of Arizona, 1989.
21. P. M. Gresho, S. T. Chan, R. L. Lee and C. D. Upson, 'A modified finite element method for solving the time-dependent, incompressible Navier–Stokes equations. Part 1: Theory', *Int. j. numer. methods fluids*, **4,** 557–598 (1984).